BIOINSPIRED MATERIALS

珍珠层

Synthetic nacre by predesigned matrix-directed mineralization

预设计基质定向矿化合成珍珠层

Li-Bo Mao,[1,2] Huai-Ling Gao,[1,2] Hong-Bin Yao,[1,2] Lei Liu,[1,2,3] Helmut Cölfen,[3] Gang Liu,[4] Si-Ming Chen,[1,2] Shi-Kuo Li,[1,2] You-Xian Yan,[1,2] Yang-Yi Liu,[1,2] Shu-Hong Yu[1,2,4]*

Although biomimetic 仿生的 designs are expected to play a key role in exploring future structural materials, facile fabrication of bulk biomimetic materials under ambient 外界的、周围的 conditions remains a major challenge. Here, we describe a mesoscale 中尺度的 "assembly-and-mineralization" approach inspired by the natural process in mollusks 贝类、软体动物 to fabricate bulk synthetic nacre that highly resembles both the chemical composition and the hierarchical 分层的 structure of natural nacre. The millimeter-thick synthetic nacre consists of alternating organic layers and aragonite 霰Xian石、文石 platelet layers (91 weight percent) and exhibits good ultimate strength and fracture toughness. This predesigned matrix-directed mineralization method represents a rational strategy for the preparation of robust composite materials with hierarchically ordered structures, where various constituents are adaptable, including brittle and heat-labile materials.

Biological materials are built from limited components, but their mechanical performances, such as strength and toughness, are far beyond their artificial counterparts. The secret of success is their hierarchically ordered structure at multiscale 多尺度的 levels (*1*–*4*). The most studied model among these biological materials is the nacreous part in some mollusk shells that consists of about 95 weight % (wt %) of brittle aragonitic $CaCO_3$ and 5 wt % of organic materials (*5*). Mollusks produce nacre by first generating several layers of insoluble β-chitin matrix filled with silk fibroin 蚕丝蛋白 gel (*6*). Then aragonite cores form on the surface of the matrix at the nucleation sites (*7*), followed by lateral 横向的 growth in the confined space of adjacent organic layers, which finally leads to a Voronoi pattern 冯洛诺伊图 (*5*). These aragonite platelets, despite their single-crystal diffraction pattern, are not perfect single crystals but essentially consist of nanograins with the same crystallographic orientation (mesocrystals 介晶), whereby the platelets are not as fragile as perfect single crystals (*8*). The mature nacre has a "brick-and-mortar 砂浆" microstructure where aragonite platelet layers are bound by an organic matrix (*3*). Through a number of such structural designs and toughening mechanisms at multiscale levels (*2*, *9*, *10*), nacre reconciles its toughness and strength, which are mutually exclusive in most artificial materials (*11*).

介晶，由许多个小晶粒有序组成的一个大晶体，由于小晶粒晶格趋向一致度相当高，所以组成的大晶体接近于单晶结构。既具有像液体一样的流动性和连续性，又具有晶体一样的各向异性。

In contrast to biological materials, the evolution of synthetic structural materials has been achieved predominately by developing new synthetic compounds rather than optimizing the micro/nanostructures of existing materials. Therefore, bioinspired designs of multiscale structures are promising for developing surpassing structural materials (*5*, *12*). However, the fabrication of bulk biomimetic materials is by no means a low-hanging fruit 唾手可得 (*12*), because it is hard to balance the well-organized hierarchical structure and the efficiency. For nacre, the strategies used for producing its artificial counterparts can be categorized into three groups: the layer-by-layer technique (*13*–*16*), the self-assembly technique (*17*–*20*), and the slurry-based freeze-casting/magnetic-field-assisted slip-casting and sintering 烧结 technique (*21*–*25*). Although these artificial materials are to some extent similar to natural nacre, the state-of-the-art 最先进的 techniques focus on mimicking 模仿 the layered structure by anisotropic assembly of building blocks but have not achieved the fabrication of bulk synthetic nacre via a mineralization strategy that is adopted by many living creatures to produce biomaterials, including nacre (*5*–*7*). Furthermore, the high-temperature heat treatment (*22*–*25*) excludes many heat-labile materials and thus substantially limits their applications.

Considering that mollusks build their nacre by the mineralization in a preformed laminated 层状的 matrix (*5*), we developed a consecutive assembly-and-mineralization process (Fig. 1) to produce synthetic nacre by a mesoscale approach where the nanostructure and the microstructure are controlled simultaneously. Through a freezing-induced assembly process (Fig. 1, A and B, and fig. S1), a chitosan matrix with predesigned laminated structure is fabricated (fig. S2, A, B, D, and E). Then the matrix is acetylated (Fig. 1C) and transformed to β-chitin to avoid unwanted swelling or dissolution (fig. S2, C and E, and table S1). The acetylated 乙酰化 matrix is mineralized in a peristaltic pump-driven circulatory system via the decomposition of $Ca(HCO_3)_2$ in the presence of polyacrylic acid (PAA) 聚丙烯酸 and Mg^{2+} (Fig. 1D). Then the final material is obtained by silk fibroin infiltration and hot-pressing of the mineralized matrix. The thickness of the bulk synthetic nacre is about 1 to 2 mm, based on the thickness of the original chitin matrix (Fig. 2B), which can be further increased by using thicker matrix (Fig. 1B). The $CaCO_3$ in the synthetic nacre is aragonite (fig. S3), which is attributed to the control of the additives (*26*).

Typically, as the size of the three-dimensional (3D) matrix increases, the mass transfer throughout

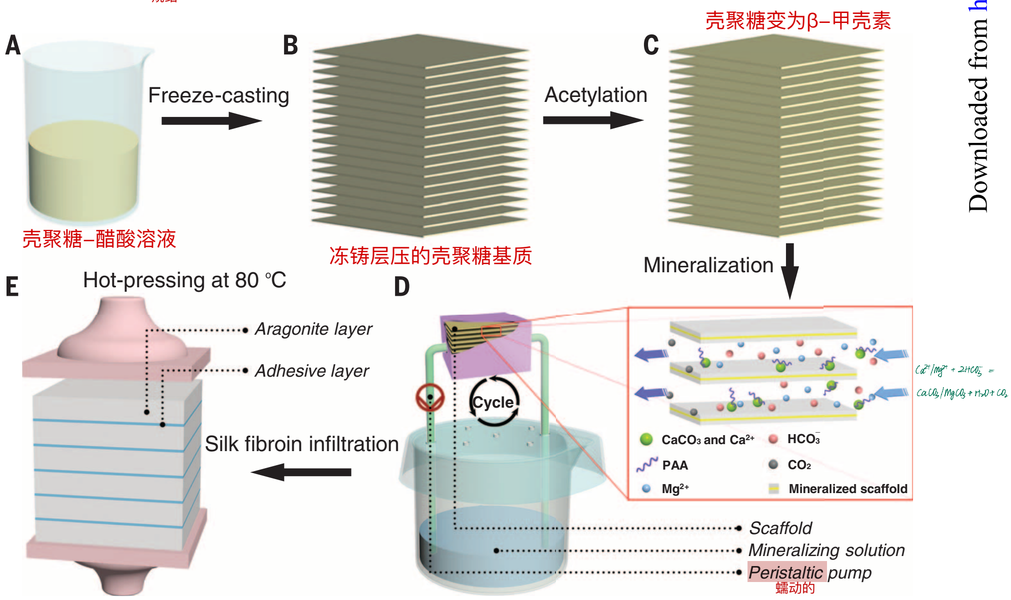

Fig. 1. Fabrication scheme of the synthetic nacre. (**A**) Starting solution, chitosan/acetic acid solution. (**B**) Freeze-casted laminated chitosan matrix. (**C**) Matrix after acetylation, where chitosan is converted to β-chitin. (**D**) Mineralization of the matrix. Fresh mineralizing solution is pumped to flow through the space between the layers in the matrix, bringing in Ca^{2+}, Mg^{2+}, HCO_3^-, and PAA for mineralization and taking out excess CO_2. $CaCO_3$ precipitates onto the layers and CO_2 diffuses into the air through the pin holes in the paraffin 石蜡 film. (**E**) Laminated synthetic nacre is obtained after silk fibroin infiltration and hot-pressing.

---

[1]Division of Nanomaterials and Chemistry, Hefei National Laboratory for Physical Sciences at the Microscale, University of Science and Technology of China, Hefei, 230026, China. [2]Chinese Academy of Sciences, Center for Excellence in Nanoscience, Collaborative Innovation Center of Suzhou Nano Science and Technology, Hefei Science Center, Department of Chemistry, University of Science and Technology of China, Hefei, 230026, China. [3]University of Konstanz, Physical Chemistry, Universitätsstraße 10, D-78457 Konstanz, Germany. [4]National Synchrotron Radiation Laboratory, University of Science and Technology of China, Hefei, 230029, China.
*Corresponding author. Email: shyu@ustc.edu.cn

一般情况下，随着三维(3D)基质尺寸的增大，整个基质的传质难度会加大，这意味着整个基质的矿化会受到阻碍。

the matrix will be more difficult, which means the mineralization of the whole matrix will be retarded. In our work, this problem is overcome through experimental designs. There is enough space between the chitin layers of the matrix, which is indispensable for the mass transfer across the whole laminated structure and thus facilitates the thorough mineralization of the matrix. Otherwise, a dense mineral shell will form on the surface and obstruct the mineralization process inside (fig. S4A). To promote the mass transfer in the matrix further, the precipitation of $CaCO_3$ is achieved by the decomposition of calcium bicarbonate rather than the gas-diffusion method because the spontaneous diffusion of CO_2 (fig. S4B) is much slower than the direct pump-driven injection of $Ca(HCO_3)_2$ (fig. S4, C and D). Consequently, the whole matrix mineralizes to the extent that the resulting synthetic nacre contains as much as 91 wt % of $CaCO_3$, which is quite comparable to natural nacre (5). Because of the high inorganic content, the synthetic nacre exhibits high stability in water without noticeable swelling (movie S1). More important, while the growth of natural nacre takes months or even years, only 2 weeks are needed for the preparation of the bulk synthetic nacre whose composition is almost the same as natural nacre (figs. S3 and S5) (5).

减缓

表面形成的致密矿物会阻碍内部的矿化过程。

生长周期：
天然珍珠层–几月到几年
合成珍珠层–2周

The synthetic nacre shares striking similarities with natural nacre from the shell of mollusk such as *Anodonta woodiana*. The fracture surface of the bulk synthetic nacre reveals a laminated nacre-like microstructure (Fig. 2, A to D; fig. S6, A and B; and movie S2). The thickness of the alternating aragonite and organic layers is 2 to 4 μm and 100 to 150 nm, respectively. Hence, it is supposed that the Bragg diffraction–induced structural coloration (5) of the synthetic nacre is not in the visible range (Fig. 2B). Each mineral layer is made up of tilelike aragonite platelets and exhibits a structure similar to Voronoi pattern, which is typically observed in natural nacre (Fig. 2, E and F) (5). However, as the mineralization conditions are complicated and the control of the process in our experiment is not as good as the biomineralization process in mollusks, the Voronoi patterns are not so perfect in the synthetic nacre (red circles in Fig. 2F). The formation of this pattern can be ascribed to the growth mechanism that $CaCO_3$ selectively precipitates at some nucleation sites (white arrowheads in Fig. 2F) that were identified to be rich in carboxyl groups (7), and then these initial crystals grow laterally on the chitin layers until they meet each other to form a boundary (fig. S6C and movie S3). As the matrix gradually mineralizes, the chitin layers are assimilated by the minerals, probably because of electrostatic attraction (figs. S7 and S8), whereas the infiltrated silk fibroin forms the organic layers between the aragonite layers (fig. S9). Both the average size and the aspect ratio of the aragonite platelets in the synthetic nacre are significantly larger than that in *A. woodiana* nacre (fig. S10), which greatly affect the properties of the as-fabricated nacre-like materials (19).

河蚌

瓦片状的

CaCO3在核点选择性沉积，被羧酸基团识别，然后最初的晶体横行生长，直到与相邻的晶体相遇形成边界。

The aragonite platelets in the synthetic nacre consist of attached nanograins with diameters ranging from 10 to 100 nm (Figs. 2H and 3A), in accordance with those in natural nacre (Fig. 2G) (8). Further analysis of the nanograins reveals the crystallographic features of the platelets (Fig. 3, B to D). The single-crystal–like fast Fourier transform (FFT) patterns (Fig. 3, C and D) of the boundary areas (Fig. 3B) indicate the orientation continuity between adjacent nanograins in a single platelet, because the precipitation of $CaCO_3$ in our experiment should follow a nonclassical crystallization mechanism (27, 28). Although the aragonite platelets are mesocrystals (27) due to the orientation continuity of individual nanoparticles, the aragonite platelets in a layer grow independently (fig. S6C and movie S3), and thus the crystal orientation degree of the whole synthetic nacre is as low as ~9%. Therefore, a single aragonite layer shows distinctive dark and bright mosaics under cross-polarized light where the brightness of these tiles depends on their orientations (Fig. 3E and fig. S10A). In addition, the adjacent layers do not contact each other during the mineralization process (fig. S4D), and thus the orientations of the adjacent layers are also self-reliant. Consequently, the x-ray diffraction pattern of the synthetic nacre is in line with *A. woodiana* nacre powder, where the aragonite platelets are randomly oriented, but not bulk *A. woodiana* nacre, where all the platelets have near-parallel (002) planes (fig. S3).

纳米晶

傅里叶快速变换

The microscopic mechanical properties of the synthetic nacre are comparatively studied by nanoindentation (NI). Long cracks are induced by the indents in both monolithic calcite and aragonite, and then they propagate easily along the cleavage planes (8). In comparison, no microscopic crack or crack propagation is observed in *A. woodiana* nacre or the synthetic nacre (Fig. 4A). The excellent antiflaw performance of both composites can

单片方解石

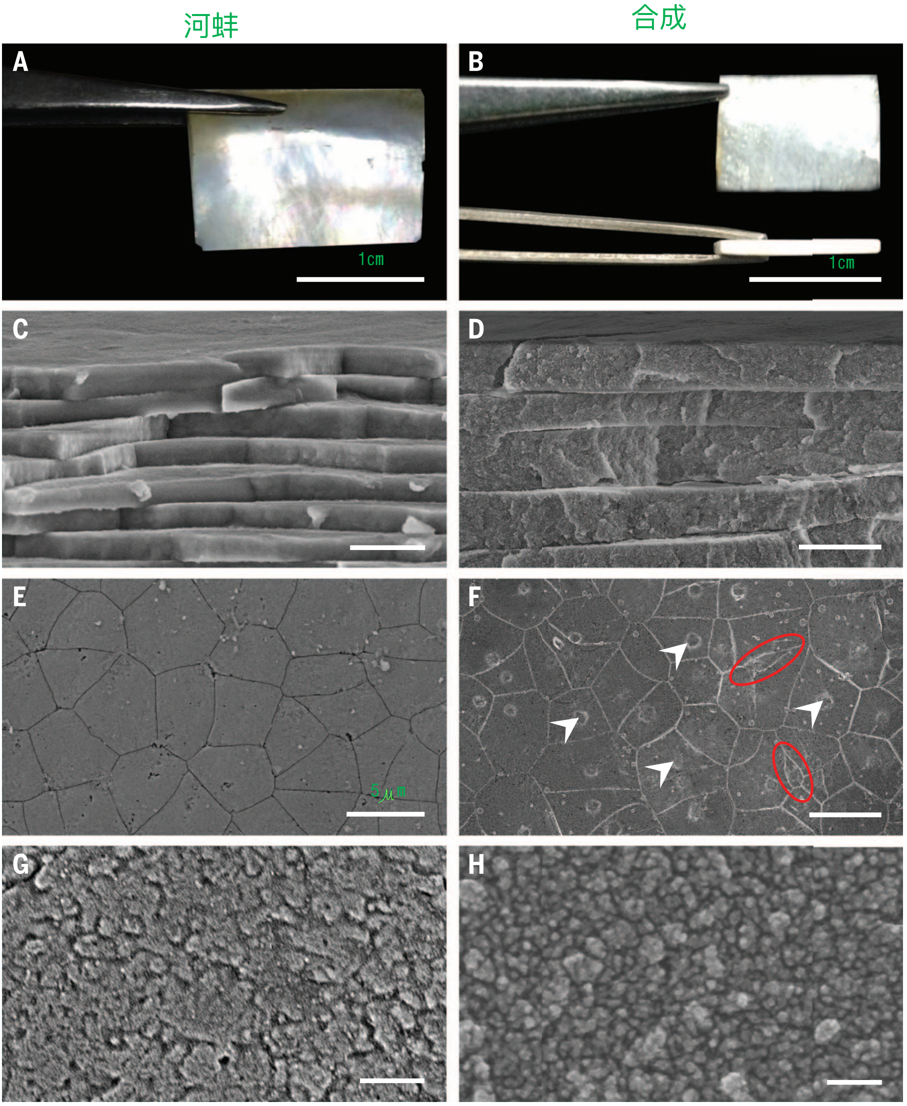

Fig. 2. The comparison of the appearance and multiscale structure between natural and synthetic nacre. (**A**) *A. woodiana* nacre. (**B**) Bulk synthetic nacre. (**C** and **D**) Fracture surface of (C) *A. woodiana* nacre and (D) synthetic nacre. (**E** and **F**) Voronoi pattern of the aragonite layer in (E) *A. woodiana* nacre and (F) synthetic nacre. (**G** and **H**) Enlarged micrographs of the aragonite platelet of (G) *A. woodiana* nacre and (H) synthetic nacre. Scale bars are 1 cm, 1 cm, 3 μm, 3 μm, 5 μm, 100 μm, 100 nm, and 100 nm for (A) to (H), respectively.

be attributed to their unique connected-nanograin structure (Fig. 2, G and H) (*29*). Like the nanograins in natural nacre that are bound by organics like proteins (*8*), it is suggested that the nanograins in the synthetic nacre (Fig. 3A) also contain or are connected by the added PAA molecules, which can strongly interact with $CaCO_3$ (*30*). Furthermore, the assimilated chitin shreds embedded in the aragonite layers (fig. S8, C and D) provide additional binding components and act as buffer zones for internal stress (*31*). Consequently, although there are weak cleavage planes in abiotic single crystals, there is no cleavage plane in these mesocrystals; the energy can be dissipated efficiently via breaking the bonding between nanograins, and the nanocracks in these mesocrystals can be localized (*8*, *32*). Using the Olive-Pharr model to analyze the data obtained from the NI tests, it can be found that the synthetic nacre undergoes losses in its elastic modulus and hardness (fig. S11), which is ascribed mainly to the thick grain boundaries between the aragonite nanograins (Fig. 3A, fig. S12, and the calculation in the supplementary materials). It is estimated that the volume fraction of organic components in the synthetic nacre is about 14%, whereas in *A. woodiana* nacre it is less than 8%. Accordingly, the macroscopic density of the synthetic nacre is significantly smaller than that of aragonite and *A. woodiana* nacre (fig. S13). Moreover, because the organic components in the grain boundaries are sensitive to water, the elastic modulus of the fully hydrated synthetic nacre decreases, whereas the ultimate strain increases remarkably (fig. S14).

无生命的、非生物的

As the composition and the hierarchical structure of the synthetic nacre bear a striking resemblance to natural nacre, the macroscopic mechanical properties of the synthetic nacre are also superior to pure aragonite and its related composites and comparable to that of natural nacre (Fig. 4B; see also fig. S13). The rising crack-extension resistance curves of both the synthetic and natural nacre indicate extrinsic toughening mechanisms in these materials (Fig. 4C). The reinforced performance of the synthetic nacre is attributed to the structural features at multiscale levels where the organic components play a key role (figs. S15 and S16). The assembled-nanograin architecture and the organic binders (e.g., PAA and chitin) by which energy can be dissipated and nanocracks can be localized are the structural basis of the macroscopic performance of the synthetic nacre. Moreover, the laminated nacre-like structure leads to crack branching, crack deflection, crack blunting, crack trapping in the organic layers, and platelet bridging (Fig. 4, D and E; see also fig. S17, E and F) (*33*). Some microscopic features, such as platelet waviness and dovetail structure that are responsible for the hardening and damage tolerance in natural nacre (*34*), have also been observed in the synthetic nacre (fig. S18). In addition, the delamination process is retarded by the infiltrated silk fibroin binding layers and thus further dissipates energy (Fig. 4F; see also fig. S9, A and B). However, because their microstructures (fig. S19) as well as the suggested micromechanical models are not exactly the same

B右上角

B左下角

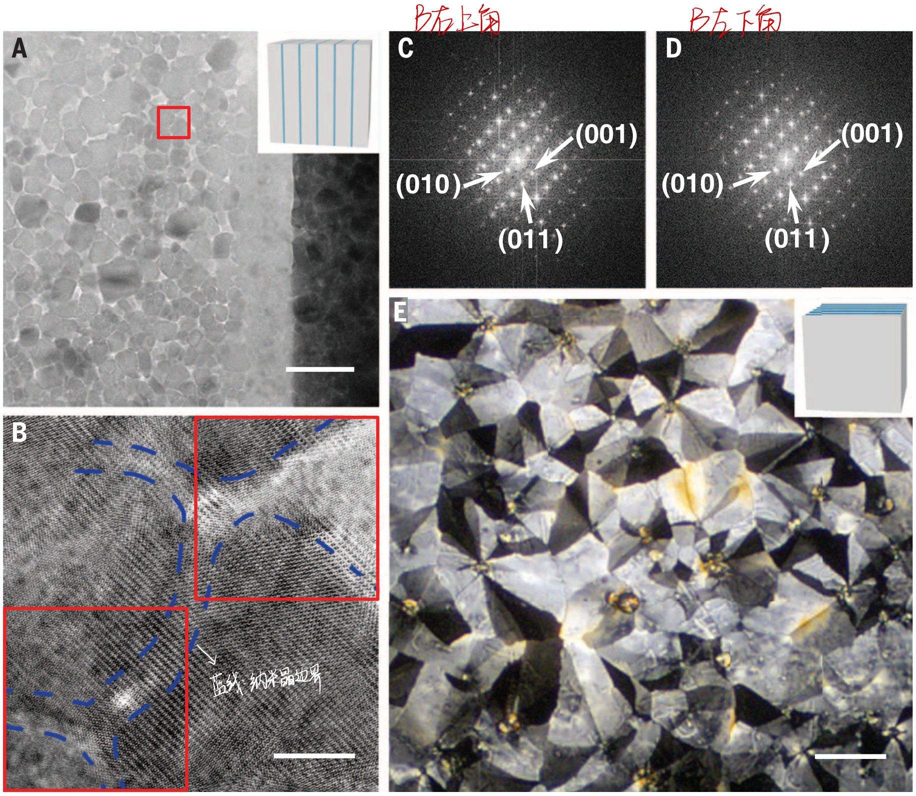

十字偏振光照片

Fig. 3. Crystallographic structure of the synthetic nacre. (**A**) Cross-sectional transmission electron microscope (TEM) image of the synthetic nacre. The inset shows the view direction. (**B**) High-resolution TEM (HRTEM) image of the selected area in (A). The boundaries of the nanograins are marked with dashed blue lines. (**C** and **D**) FFT of the selected squares denoted by red lines in (B), where (C) corresponds to the top right square and (D) the bottom left. (**E**) Optical micrograph of the aragonite layer under cross-polarized light, where the inset shows the view direction. Scale bars are 100 nm, 10 nm, and 50 μm for (A), (B), and (E), respectively.

抗裂纹扩展曲线

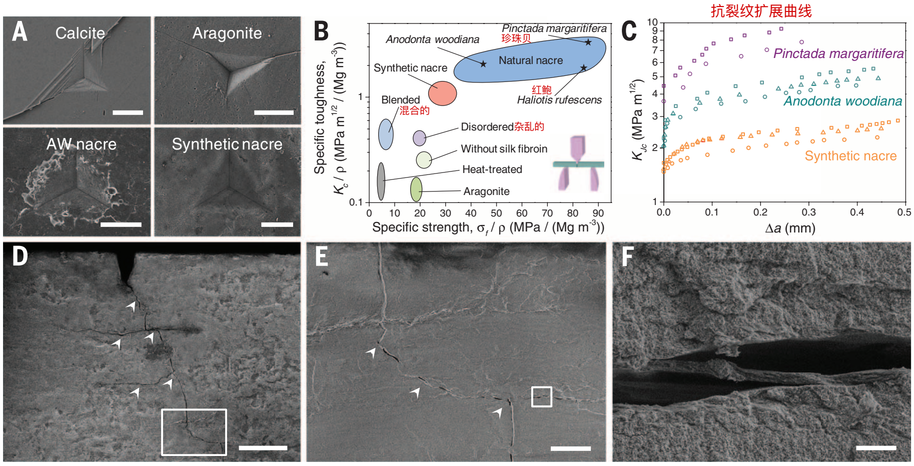

Fig. 4. Mechanical properties of the synthetic nacre. (**A**) Residual indents of the Berkovich diamond tip in abiotic minerals, *A. woodiana* (AW) nacre, and the synthetic nacre. (**B**) Specific fracture toughness versus specific ultimate flexural strength, illustrating the mechanical performance of the synthetic nacre, natural nacre, pure aragonite, and their related materials. (**C**) Rising crack-extension resistance curves (evaluated by the steady-state fracture toughness K_{Jc}) of the synthetic nacre and some natural nacre. (**D**) Profile of the fractured synthetic nacre showing the multiple toughening mechanisms. (**E**) Crack deflection between layers and crack branching [enlarged micrograph of the marked area in (D)]. (**F**) Crack-induced interlamellar debonding in the synthetic nacre [enlargement of the marked area in (E)]. The data of *Pinctada margaritifera* and *Haliotis rufescens* are adapted from (*35*) and (*36*). Scale bars are 10, 200, 40, and 2 μm for (A), (D), (E), and (F), respectively.

锯齿形缺口

偏向

(fig. S20), the mechanical properties of the synthetic nacre are still not as good as that of natural nacre (*35*, *36*) (Fig. 4, B and C). Due to the larger aspect ratio of the aragonite platelets in the synthetic nacre, the platelets exhibit a "partly pullout" behavior, which leads to lower crack-resistance capability.

Because the precipitation of the second phase onto the matrix relies on electrostatic force, $CaCO_3$ and chitin can be substituted by other precursors with opposite charges to make superior composites such as engineering ceramics (*21*–*24*) (figs. S21 and S22). Besides, as the dependence of properties of the composite materials on the characteristic length of their periodic microstructure (*37*), the mechanical performance of these materials can be optimized by adjusting the properties of the original matrix (*38*), which affect both the amount of electrostatically absorbed precipitates and the density of the nucleation sites. The fabrication of the laminated synthetic nacre is not a special case; there are other techniques, such as programmable 3D printing, for constructing predesigned macroscopic matrices that can be readily incorporated with our strategy to produce composite materials. Moreover, this strategy is also adaptable for fabricating robust bulk materials with brittle and heat-labile components (fig. S21B). Given the importance of nano- and microscopic structures for the materials performance, we thus anticipate that our method can be extended to produce various composite materials with unique properties.

REFERENCES AND NOTES

1. P. Fratzl, R. Weinkamer, *Prog. Mater. Sci.* **52**, 1263–1334 (2007).
2. B. Ji, H. Gao, *Annu. Rev. Mater. Res.* **40**, 77–100 (2010).
3. J. Wang, Q. Cheng, Z. Tang, *Chem. Soc. Rev.* **41**, 1111–1129 (2012).
4. M. A. Meyers, J. McKittrick, P.-Y. Chen, *Science* **339**, 773–779 (2013).
5. H.-B. Yao, J. Ge, L.-B. Mao, Y.-X. Yan, S.-H. Yu, *Adv. Mater.* **26**, 163–188 (2014).
6. A. G. Checa, J. H. E. Cartwright, M.-G. Willinger, *Proc. Natl. Acad. Sci. U.S.A.* **106**, 38–43 (2009).
7. L. Addadi, D. Joester, F. Nudelman, S. Weiner, *Chemistry* **12**, 980–987 (2006).
8. Z. Huang, X. Li, *Sci. Rep.* **3**, 1693 (2013).
9. P.-Y. Chen *et al.*, *J. Mech. Behav. Biomed.* **1**, 208–226 (2008).
10. I. Jäger, P. Fratzl, *Biophys. J.* **79**, 1737–1746 (2000).
11. R. O. Ritchie, *Nat. Mater.* **10**, 817–822 (2011).
12. U. G. K. Wegst, H. Bai, E. Saiz, A. P. Tomsia, R. O. Ritchie, *Nat. Mater.* **14**, 23–36 (2015).
13. Z. Tang, N. A. Kotov, S. Magonov, B. Ozturk, *Nat. Mater.* **2**, 413–418 (2003).
14. A. Finnemore *et al.*, *Nat. Commun.* **3**, 966 (2012).
15. Y. Kim *et al.*, *Nature* **500**, 59–63 (2013).
16. T. Kato, T. Suzuki, T. Irie, *Chem. Lett.* **29**, 186–187 (2000).
17. L. J. Bonderer, A. R. Studart, L. J. Gauckler, *Science* **319**, 1069–1073 (2008).
18. P. Laaksonen *et al.*, *Angew. Chem. Int. Ed.* **50**, 8688–8691 (2011).
19. P. Das *et al.*, *Nat. Commun.* **6**, 5967 (2015).
20. B. Zhu *et al.*, *Angew. Chem. Int. Ed.* **54**, 8653–8657 (2015).
21. H. Le Ferrand, F. Bouville, T. P. Niebel, A. R. Studart, *Nat. Mater.* **14**, 1172–1179 (2015).
22. S. Deville, E. Saiz, R. K. Nalla, A. P. Tomsia, *Science* **311**, 515–518 (2006).
23. E. Munch *et al.*, *Science* **322**, 1516–1520 (2008).
24. F. Bouville *et al.*, *Nat. Mater.* **13**, 508–514 (2014).
25. H. Bai, Y. Chen, B. Delattre, A. P. Tomsia, R. O. Ritchie, *Sci. Adv.* **1**, e1500849 (2015).
26. F. Zhu *et al.*, *Chem. Asian J.* **8**, 3002–3009 (2013).
27. M. Niederberger, H. Cölfen, *Phys. Chem. Chem. Phys.* **8**, 3271–3287 (2006).
28. H. Cölfen, M. Antonietti, *Mesocrystals and Nonclassical Crystallization* (Wiley, Chichester, UK, 2008).
29. J. Wang, L. L. Shaw, *Biomaterials* **30**, 6565–6572 (2009).
30. D. Gebauer, H. Cölfen, A. Verch, M. Antonietti, *Adv. Mater.* **21**, 435–439 (2009).
31. S. Weiner, L. Addadi, H. D. Wagner, *Mater. Sci. Eng. C* **11**, 1–8 (2000).
32. J. Seto *et al.*, *Proc. Natl. Acad. Sci. U.S.A.* **109**, 3699–3704 (2012).
33. Y. Shao, H. P. Zhao, X. Q. Feng, H. Gao, *J. Mech. Phys. Solids* **60**, 1400–1419 (2012).
34. F. Barthelat, H. Tang, P. Zavattieri, C. Li, H. Espinosa, *J. Mech. Phys. Solids* **55**, 306–337 (2007).
35. R. Z. Wang, Z. Suo, A. G. Evans, N. Yao, I. A. Aksay, *J. Mater. Res.* **16**, 2485–2493 (2001).
36. R. Rabiei, S. Bekah, F. Barthelat, *Acta Biomater.* **6**, 4081–4089 (2010).
37. P. Fratzl, O. Kolednik, F. D. Fischer, M. N. Dean, *Chem. Soc. Rev.* **45**, 252–267 (2016).
38. S. Deville, *Adv. Eng. Mater.* **10**, 155–169 (2008).

ACKNOWLEDGMENTS

The authors thank Y. Tian, L. Chen, and Y. Guan for computed tomography imaging, and L. Wang for sample preparation. The authors also thank Y. Ni and Z. Song for discussion about mechanical models. This work was supported by the National Natural Science Foundation of China (grant 21431006), the Foundation for Innovative Research Groups of the National Natural Science Foundation of China (grant 21521001), the National Basic Research Program of China (grants 2014CB931800 and 2013CB931800), the Users with Excellence and Scientific Research Grant of Hefei Science Center of CAS (2015HSC-UE007 and 2015SRG-HSC038), and Key Research Program of Frontier Sciences, CAS (Grant QYZDJ-SSW-SLH036). Data are available in the supplementary materials.

SUPPLEMENTARY MATERIALS

www.sciencemag.org/content/354/6308/107/suppl/DC1
Materials and Methods
Figs. S1 to S22
Table S1
Movies S1 to S3
References (*39*–*49*)

17 April 2016; accepted 4 August 2016
Published online 18 August 2016
10.1126/science.aaf8991

COGNITION

Great apes anticipate that other individuals will act according to false beliefs

**Christopher Krupenye,[1]*† Fumihiro Kano,[2,3]*† Satoshi Hirata,[2]
Josep Call,[4,5] Michael Tomasello[5,6]**

Humans operate with a "theory of mind" with which they are able to understand that others' actions are driven not by reality but by beliefs about reality, even when those beliefs are false. Although great apes share with humans many social-cognitive skills, they have repeatedly failed experimental tests of such false-belief understanding. We use an anticipatory looking test (originally developed for human infants) to show that three species of great apes reliably look in anticipation of an agent acting on a location where he falsely believes an object to be, even though the apes themselves know that the object is no longer there. Our results suggest that great apes also operate, at least on an implicit level, with an understanding of false beliefs.

Central to everything that makes us human—including our distinctive modes of communication, cooperation, and culture—is our theory of mind (TOM). TOM is the ability to impute unobservable mental states, such as desires and beliefs, to others (*1*, *2*). For nearly four decades, a cardinal question in psychology has concerned whether nonhuman animals, such as great apes, also possess this cognitive skill (*1*, *3*). A variety of nonverbal behavioral experiments have provided converging evidence that apes can predict others' behavior, not simply based on external cues but rather on an understanding of others' goals, perception, and knowledge (*3*, *4*). However, it remains unclear whether apes can comprehend reality-incongruent mental states (e.g., false beliefs) (*3*), as apes have failed to make explicit behavioral choices that reflect false-belief understanding in several food-choice tasks (*4*–*6*). False-belief understanding is of particular interest because it requires recognizing that others' actions are driven not by reality but by beliefs about reality, even when those beliefs are false.

In human developmental studies, it is only after age 4 that children pass traditional false-belief tests, in which they must explicitly predict a mistaken agent's future actions (*7*). However, recent evidence has shown that even young infants can pass modified false-belief tests that involve the use of simplified task procedures and spontaneous-gaze responses as measures [e.g., violation of expectation (*8*), anticipatory looking (*9*, *10*)]. For example, anticipatory looking paradigms exploit

---

[1]Department of Evolutionary Anthropology, Duke University, Durham, NC 27708, USA. [2]Kumamoto Sanctuary, Wildlife Research Center, Kyoto University, Kumamoto, Japan. [3]Primate Research Institute, Kyoto University, Inuyama, Japan. [4]School of Psychology and Neuroscience, University of St Andrews, St Andrews, UK. [5]Department of Developmental and Comparative Psychology, Max Planck Institute for Evolutionary Anthropology, Leipzig, Germany. [6]Department of Psychology and Neuroscience, Duke University, Durham, NC 27708, USA.
*These authors contributed equally to this work. **†Corresponding author. Email: ckrupenye@gmail.com (C.K.); fkanou@gmail.com (F.K.)**

Synthetic nacre by predesigned matrix-directed mineralization

Li-Bo Mao, Huai-Ling Gao, Hong-Bin Yao, Lei Liu, Helmut Cölfen, Gang Liu, Si-Ming Chen, Shi-Kuo Li, You-Xian Yan, Yang-Yi Liu and Shu-Hong Yu (August 18, 2016)

Science **354** (6308), 107-110. [doi: 10.1126/science.aaf8991]
originally published online August 18, 2016

Editor's Summary

Making nacre shine in the lab

Many of the materials that animals use to make shells and skeletons are built with brittle or soft molecules. They owe their amazing mechanical properties to their layered construction, which is a challenge for synthetic fabrication. Pearly nacre, for example, has proved challenging to make owing to its complex structure of aragonite crystals in an organic matrix. Using an assembly-and-mineralization approach, Mao *et al.* have managed to fabricate nacre in the laboratory (see the Perspective by Barthelat). First, a layered, three-dimensional chitosan matrix is made, within which aragonite nanocrystals are precipitated from a solution containing calcium bicarbonate.

Science, this issue p. 107; see also p. 32

Science (print ISSN 0036-8075; online ISSN 1095-9203) is published weekly, except the last week in December, by the American Association for the Advancement of Science, 1200 New York Avenue NW, Washington, DC 20005. Copyright 2016 by the American Association for the Advancement of Science; all rights reserved. The title *Science* is a registered trademark of AAAS.